ACS Energy LETTERS

http://pubs.acs.org/journal/aelccp

Integration of Thermoelectric Conversion with Reverse Electrodialysis for Mitigating Ion Concentration Polarization and Achieving Enhanced Output Power Density

Changjia Zhu, Xiuhui Zuo, Weipeng Xian, Qing Guo, Qing-Wei Meng, Sai Wang, Shengqian Ma, and Qi Sun*

Cite This: *ACS Energy Lett.* 2022, 7, 2937−2943

Read Online

ACCESS | Metrics & More | Article Recommendations | Supporting Information

ABSTRACT: **Concentration polarization (CP) is a ubiquitous phenomenon in membrane separation that is possibly responsible for the decline in overall efficiency. However, no quantitative connection between the key membrane parameters and the degree of CP has been established. In this study, the variation in permselectivity during CP was comprehensively elucidated using isostructural covalent organic framework (COF) membranes with varied charge densities. A volcano-like plot of output power density against charge population was obtained, in contrast to the conventional presumptions regarding an increase in the membrane charge density leading to an enhancement in permselectivity, and a consequent increase in osmotic voltage. The CP-induced detrimental effects were considerably mitigated by imposing a temperature gradient on the solutions, which led to an increase in the thermophoretic mobility of ions. The reverse electrodialysis (RED) device with alleviated CP yielded an output power density of up to 24.7 mW cm^{-2} with a temperature difference of ∼40 K; this value far exceeds the commercial benchmark, thus establishing a new criterion for RED batteries. These results outline a previously undiscovered benefit for linking thermoelectric conversion and RED to realize advanced energy-conversion technologies.**

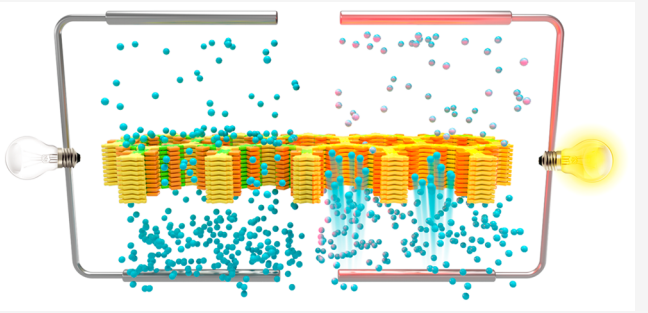

Ion concentration polarization (ICP) is a fundamental electrochemical phenomenon that induces a diffusion boundary layer adjacent to a membrane. ICP is reflected by the formation of an ion-depletion zone at the surface of a permselective membrane facing the concentrated solution, and an ion-enrichment zone comprising the transmitted counter-ions at its opposite side.[1,2] Therefore, ICP diminishes the driving force that enables transmembrane transport of preferential ions, which inhibits the practical applications of numerous membrane-based separation processes.[3,4]

The extraction of osmotic energy has been increasingly focused on in the past decade.[5−12] Researchers have predicted that 0.8 kW of Gibbs free energy can be obtained from the controlled mixing of per cubic meter of river water and seawater, which is sufficient to satisfy most of the energy requirements for society.[13] Reverse electrodialysis (RED) has proven to be an efficient technology for directly harvesting this energy.[14−17] Despite enormous research efforts, full-scale utilization of RED has thus far failed in realizing satisfactory output power densities, limiting its practical application; this is primarily because of the concentration polarization (CP) of ionic membranes, which are at the heart of RED-based saline batteries.[18−20] Among the various parameters that determine the performance of ionic membranes, charge density is a particularly critical factor. Increasing the charge population strengthens the overlapped electrical double layers (EDLs) by attracting more counterions, thereby attenuating the leakage of co-ions, which can theoretically increase the magnitude of the electric potential and ionic conductance in the membrane pores.[21,22] However, this process may aggravate the ICP,

Received: July 26, 2022
Accepted: August 9, 2022

https://doi.org/10.1021/acsenergylett.2c01681
ACS Energy Lett. 2022, 7, 2937−2943

resulting in a drop in current and potential, which in turn deteriorates the maximum output power density.[23,24] Therefore, the charge population of these membranes should be judiciously optimized to maximize power generation.

A strategy for overcoming this issue was demonstrated in the present study, which involved exerting external hydrodynamic convection effects at the membrane interface, leading to the alleviation of the degree of ICP in high-ionic-density membranes during RED. Imposing a temperature gradient near the membrane was found to restrict the expansion of the ICP zone, which enabled the realization of a higher power production density (Figure 1). The small temperature gradient required to drive the ion transport could be achieved using low-grade heat sources (<100 °C), emphasizing the feasibility of this strategy. The resulting RED device integrated with thermoelectric conversion offered a power density of up to 24.7 mW cm^{-2}, with the values enhanced by up to 4 times upon introducing a temperature gradient of ∼40 K. This research provides a practical approach to weaken the ICP phenomenon while simultaneously establishing a path for recycling waste heat to enhance the energy utilization efficiency.

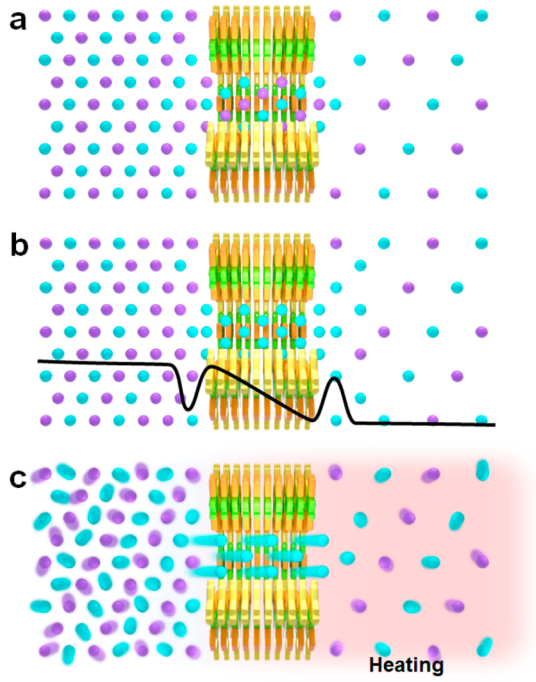

Figure 1. Illustration of ion concentration polarization phenomenon at the surface of a permselective membrane and the proposed strategy for alleviating membrane concentration polarization by imposing a temperature gradient to enhance the thermophoretic mobility of ions. (a) Ion transport through a non-permselective membrane. (b) Ion transport through a permselective membrane, which is accompanied by the occurrence of ICP and the schematic drawing of the distribution of counterions in the vicinity of a permselective membrane during ICP. (c) Ion transport through a permselective membrane with alleviated ICP by increasing the hydrodynamic convection effects via introducing a temperature gradient.

Covalent organic framework (COF) membranes were employed as ionic membranes with varied charge densities in this study. This type of material is susceptible to manipulation of its charge density without altering the underlying topology of the framework, which is a hallmark feature of reticular chemistry.[25−42] COF-BTA_xBTH_y/PAN membranes were synthesized by covalently linking triformylphloroglucinol (Tp) and terephthalohydrazide compounds on the liquid−solid interfaces of a polyacrylonitrile (PAN) ultrafiltration membrane, in accordance with our previously reported method (Figure 2 and Figure S1).[43] The charge density in the COF membranes was adjusted by varying the molar ratio of 2,2′-((2,5-di(hydrazinecarbonyl)-1,4-phenylene)bis(oxy))bis-(*N,N,N*-trimethylethan-1-aminium) iodide (BTA) and 2,5-bis(2-(dimethylamino)ethoxy)terephthalohydrazide (BTH) using a multivariate strategy. Solid-state ^{13}C nuclear magnetic resonance (^{13}C NMR), powder X-ray diffraction (PXRD) patterns, N_2 sorption isotherms, and scanning electron microscopy (SEM) images confirmed the successful preparation of ∼300-nm-thick COF membranes (Figures S2−S12). The charge densities of the membranes could be precisely manipulated in the range of 0.007−0.18 C m^{-2}, as indicated by an electron probe microanalyzer (EPMA, Tables S1 and S2).

Considering that permselectivity is a key parameter in determining the efficiency of a RED battery, the ion selectivity of COF-BTA_xBTH_y/PAN was first determined over a broad spectrum of salt concentration differences. A homemade flow cell with three reservoirs was used for these experiments. KCl solutions with concentrations ranging from 0.5 mM to 0.5 M were placed in the middle reservoir of the flow cell separated by the COF and PAN membranes, respectively, whereas 0.1 mM KCl solutions were placed in the side reservoirs. The circuit was completed with a couple of Ag/AgCl electrodes that were immersed in the side reservoirs (Figure S13). Therefore, the redox potential of Ag/AgCl as a result of the uneven potential drop at the electrode−electrolyte interface could be eliminated. The anion transference number (t_-) was calculated using eq 1:

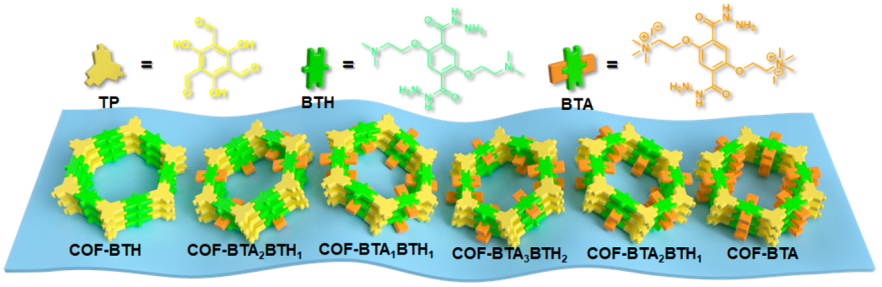

Figure 2. Schematic illustration of the isostructural covalent organic framework membranes with varied charge densities (orange structure).

https://doi.org/10.1021/acsenergylett.2c01681
ACS Energy Lett. 2022, 7, 2937−2943

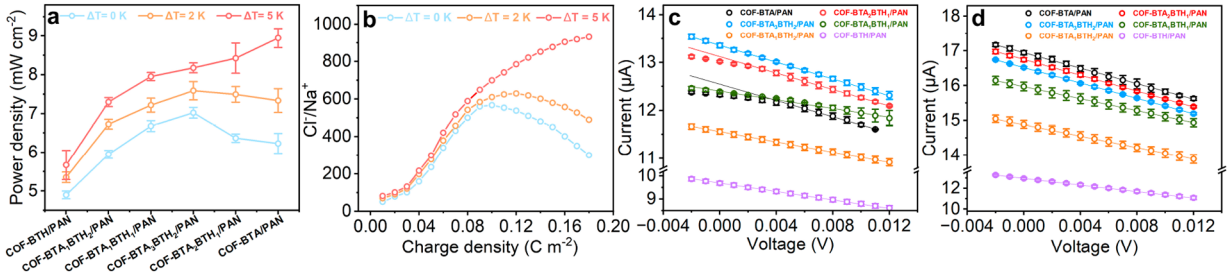

Figure 3. (a) Maximum output power achieved by the RED stack assembled with COF-BTA$_x$BTH$_y$/PAN and Nafion212, before and after the introduction of a temperature gradient. (b) Numerically simulated plots of the concentration ratio of Cl^- and Na^+ close to the channel aperture at the low-concentration side versus the charge density on the membrane, before and after the implementation of a temperature gradient. Experimental $I-V$ curves of COF-BTA$_x$BTH$_y$/PAN in various KCl solutions (c) before and (d) after the introduction of a temperature gradient of 5 K. Error bars represent standard deviation of three different measurements.

$$V_{oc} = (2t_- - 1)\frac{RT}{F}\ln\frac{a_{high}}{a_{low}} \quad (1)$$

where V_{oc}, R, T, F, and a_{high} and a_{low} are the open-circuit potential, gas constant, temperature, Faraday constant, and ion activities of high-concentration and low-concentration solutions, respectively. COF-BTA/PAN, which exhibited the highest charged-site population, did not achieve the uppermost t_- values within the investigated range of concentration differences. Instead, COF-BTA$_3$BTH$_2$/PAN, with a relatively lower charge density, exhibited superior permselectivities (Figure S14). This is in contrast to conventional expectations regarding increasing the charge density of a specific channel leading to the strength of the EDL by attracting more counterions and facilitating the enhancement of ion permselectivity and conductance. Indeed, the ionic conductivity−KCl concentration plots indicated that the conductivity of COF-BTA$_x$BTH$_y$/PAN deviated from that of the corresponding bulk solution (dashed line) at ∼0.1 M and steadily plateaued at lower concentrations; the departure from the values of bulk solutions was more apparent with increasing charge population, implying the strengthened charge governed ion transport (Figure S15).

To further examine the influence of charge density on permselectivity, these membranes were assembled into a RED stack to investigate their performance for viable osmotic energy conversion. A cation-selective membrane, Nafion212, was paired with COF-BTA$_x$BTH$_y$/PAN to form a complete battery. NaCl solution (10 mM/0.5 M) was used to mimic the ion concentrations at the river mouths. The output power density−ionic density plot of COF-BTA$_x$BTH$_y$/PAN displays a volcano-like curve (Figure 3a, light blue), and the corresponding energy conversion efficiencies are 42.8, 43.4, 43.9, 43.4, 42.0, and 40.4% for COF-BTA/PAN, COF-BTA$_2$BTH$_1$/PAN, COF-BTA$_3$BTH$_2$/PAN, COF-BTA$_1$BTH$_1$/PAN, COF-BTA$_1$BTH$_2$/PAN, and COF-BTH/PAN, respectively (also see details in the Supporting Information). The maximum values did not correspond to the membrane with the maximum charge population. Numerical calculations were performed to gain insight into the origin of this intriguing behavior, and a two-dimensional model with a channel of length 280 nm and diameter 2 nm was constructed according to the thickness and pore size of the COF membranes (Figure S16). The estimated ionic concentrations in the nanochannels revealed that although the Cl^- concentration was considerably greater than that of Na^+ in all the investigated membranes, a dependence on the population of charged sites was evident. A plot of the ratio of Cl^- and Na^+ concentrations near the channel aperture at the low-concentration side versus charge density revealed distinct differences; a trend featuring an increase and a subsequent decrease was apparent, with the maximum corresponding to the channel with a charge density of 0.09 C m^{-2} (Figure 3b). These tendencies were rationalized using membrane CP, in that the increase in surface charge density was accompanied by the attraction of more ions, which led to a larger ion-depletion zone, whereas the opposite side was more significantly populated by the transported counterions to yield an ion-enrichment zone, resulting in an appreciable decrease in the effective salinity ratio. $I-V$ curves were collected to provide evidence regarding the possible relationship between the ICP and the membranes with high charge densities. The results revealed that the profiles of COF-BTA$_x$BTH$_y$/PAN with $x/y > 2$ were nonlinear (black and red lines). An ohmic region was followed by a plateau region that transited into an over-limiting conductance region, which is characteristic of ICP.[44,45] It is worth noting that no plateau was observed in this scenario owing to the lower charge density of COF-BTA$_x$BTH$_y$/PAN ($x/y < 1.5$), which was consistent with the expected behavior (Figure 3c).

We performed numerical simulations to understand the extent of concentration polarization in response to the variations in the charge and pore densities. A set of simulation systems with charge densities and number of pores in the ranges of 0.007−0.18 C m^{-2} and 1−39, respectively, was constructed to ensure that the parameters of the fabricated COF membranes fell within the above-mentioned ranges (for instance, when the number of pores in the calculation model was 39, the corresponding pore density was slightly higher than that of the COF membranes, Figure S16). The variations in the ion distribution in response to the channel and charge densities resulting from the mixing of 0.01 and 0.5 M NaCl solutions were simulated (Table S4). As shown in Figure S17, the concentrations of anions at the entrance of the pore channels decrease, and the ion depletion boundary becomes thicker with increasing pore density; this effect is further enhanced in response to an increase in the charge density. To quantitatively describe the extent of the ICP effect, we measured the concentrations of Cl^- ions at the entrance and exit of the pore channels. The concentration differences decrease when the pore density increases, and further decrease with increasing membrane charge population. More specifically, the concentration ratio of Cl^- ions between the high-and low-concentration sides decreases from 45.9 for the system of a single channel with a charge density of 0.007 C m^{-2} to 3.4 for

https://doi.org/10.1021/acsenergylett.2c01681
ACS Energy Lett. 2022, 7, 2937−2943

the 39-channel system with a charge density of 0.18 C m^{-2} (Table S5).

Increasing the hydrodynamic flow is known to decrease the boundary layer to alleviate ICP. Therefore, a temperature gradient was imposed to enhance the hydrodynamics of the saline solutions. In particular, substantial energy is stored in the form of heated river water during the cooling process, providing tremendous promise for the implementation of this strategy.[46−59] To validate the efficiency of this approach, temperature differences were induced by briefly heating of the reservoirs filled with low-concentration solutions using a heating rod. The instantaneous temperature difference between the chambers was recorded using thermocouples, and V_{oc} was measure using Ag/AgCl electrodes. Notably, a temperature gradient of 5 K led to a linear increase in the $I-V$ curves of COF-BTA$_x$BTH$_y$/PAN with $x/y > 2$. The disappearance of the plateau region suggested the suppression of ICP after the introduction of the additional driving force induced by the temperature gradient (Figure 3d). Numerical simulations were subsequently performed to elucidate the role of the temperature gradient. The setup includes a positively charged channel (a surrogate of a COF pore channel), which is separated by warm and cold reservoirs containing 10 mM and 0.5 M NaCl solutions, respectively. The variations in the plots of Cl^-/Na^+ ratios versus charge density near the channel aperture in response to the introduced temperature gradient indicate that the temperature gradient moderately influenced the Cl^-/Na^+ ratios for the membranes with charge densities smaller than 0.09 C m^{-2}, but not for those with charge densities higher than 0.09 C m^{-2} (Figures 3b and 4, and Figure S18). The initial volcano-like curve obtained by plotting the Cl^-/Na^+ ratio and charge density transformed into a climbing profile upon the introduction of a temperature gradient of 5 K (Figure 3b). Furthermore, according to the numerical simulation, the concentration gradient of Cl^- ions between the high- and low-concentration sides increases from 3.4 to 5.0 for the 39-channel system with a charge density of 0.18 C m^{-2}, which provides evidence for the allevuatin of ICP (Table S5).

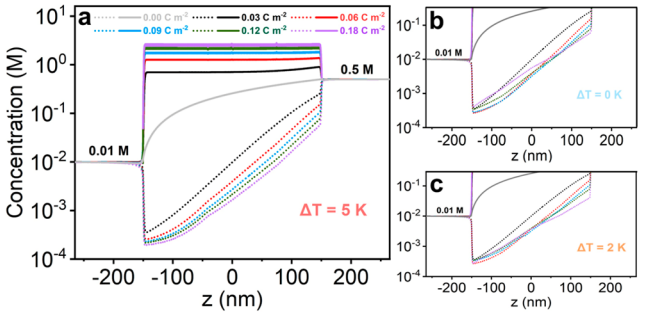

Figure 4. Numerical simulation of the impact of the imposed temperature gradients on the Na^+ (dashed line) and Cl^- (solid line) distribution in the nanochannels with various charge densities for (a), (b), and (c) are in the presence of temperature gradient of 5, 0, and 2 K, respectively.

The impact of the imposed temperature gradient on the power production density achieved by mixing 0.5 M and 10 mM NaCl for the membranes with varied charge densities via RED was subsequently quantified. To facilitate the establishment of a relationship between the variations in V_{oc} (ΔV_{oc}) and the solution temperature (ΔT), ΔT was permitted to change within ∼10 K to neglect the temperature-induced variations in the activity coefficient of ions and electrolyte potential. The time evolution profiles of ΔV_{oc} and ΔT were recorded using Ag/AgCl electrodes and a temperature recorder, respectively. The measured diffusion potential measured under open-circuit conditions was attributed to the salinity gradient and thermal-stimulus-driven ion transport, leading to a potential difference at the membrane boundary. The ionic thermoelectric response induced by a temperature gradient is characterized by the ionic Seebeck coefficient, which can be calculated using eq 2:

$$\Delta V_{oc} = -2t_- \frac{R}{F} \Delta T \ln a \tag{2}$$

where t_-, R, F, ΔT, and a are anion transference number, gas constant, Faraday constant, temperature gradient, and ion activity in low-concentration solution, respectively. Figure 5a shows the real-time evolution of ΔV_{oc} with regards to the increased temperature of low-concentration solution. Plotting ΔV_{oc} against ΔT results in linear curves (Figure 5b). The ionic Seebeck coefficient values derived from the slopes were estimated to be 0.530−0.795 mV K^{-1} for COF-BTA$_x$BTH$_y$/PAN with the values increased as the increase in charge density. This trend was rationalized by the increase of permselectivity along with the charge population increase (Figure 5c).

After experimentally demonstrating the thermoelectric conversion characteristics of the developed nanofluidic systems, the proposed concept was used to construct a prototype RED-based waste-heat energy harvester. The diffusion potentials, transmembrane currents, and power production densities were evaluated at various temperature gradients. Enhancing the temperature gradient facilitated ion transport, as demonstrated by the increase in transmembrane potential, current, and P_{max}. Notably, the increase in electric

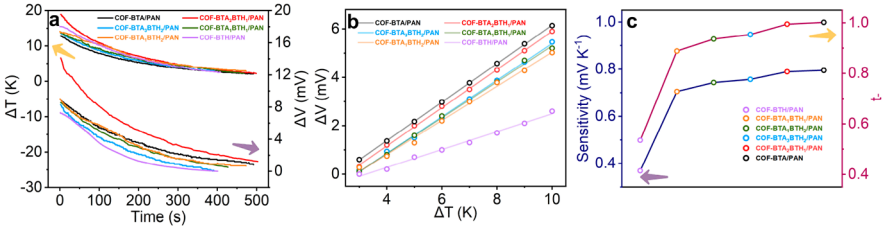

Figure 5. (a) Thermoelectric responses of COF-BTA$_x$BTH$_y$/PAN. The synchronous time evolution of ΔV_{oc} in response to the temperature changes of low-concentration solutions (the ΔT values correspond to the overlapped curves above the orange arrow). (b) Linear fits of ΔV_{oc} against ΔT according to eq 2; all the fits yielded $R^2 > 0.99$. (c) Ionic Seebeck coefficient (sensitivity) of COF-BTA$_x$BTH$_y$/PAN and the corresponding t_- values calculated using eq 2 (average of three different batch experiments).

https://doi.org/10.1021/acsenergylett.2c01681
ACS Energy Lett. 2022, 7, 2937−2943

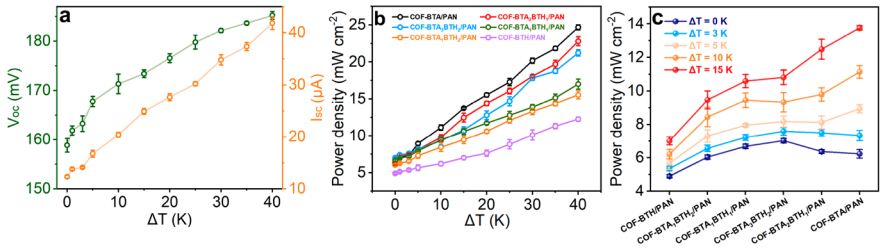

Figure 6. (a) Variation of V_{oc} and I_{sc} of the RED stack assembled by COF-BTA/PAN and Nafion212 in response to the imposed temperature gradient. (b, c) Plots of the output power density of the RED stack assembled by COF-BTA$_x$BTH$_y$/PAN and Nafion212 versus temperature gradient. Error bars represent standard deviation of three different measurements.

potential with temperature was observed to gradually flatten (Figures S19 and S20). This is because of the dependence of the thermoelectric conversion of these systems on the membrane permselectivities, which is relevant to the EDL. The thickness of the EDL can be determined using ion activity and temperature. Higher temperatures lead to thinner EDLs, which results in a decrease in ion selectivity and consequently a small potential. However, the increase in temperature increases the movement of ions, leading to a significant increase in current. Therefore, V_{oc} increased only from 158.8 to 185.2 mV, whereas I_{sc} increased remarkably from 12.3 to 41.8 μA in the case of COF-BTA/PAN subjected to a temperature gradient of 40 K (Figure 6a). Resistances were introduced to the external circuit (R_L, Figure S21) to estimate the output power density (P) using eq 3:

$$P = \frac{I^2 R_L}{4} \tag{3}$$

The evolution of the output power density with the temperature difference is depicted in Figure 6b, which reveals that the power density achieved by COF-BTA$_x$BTH$_y$/PAN increased ~2.5−4 times with a temperature gradient of 40 K. Because of the alleviation of ICP, COF-BTA/PAN afforded the highest V_{oc} and I_{sc} values among the investigated membranes, yielding a power density of 24.7 mW cm^{-2}, which is ~50-fold greater than the commercial benchmark (0.5 mW cm^{-2}) and also far exceeds the reported systems (Table S3). Notably, the volcano like plot of the output power density against the membrane charge density in converted into a plot of climbing line after introducing a temperature gradient >5 K, confirming the role of heating during the alleviation of ICP in the RED device (Figure 6c.)

To gain deeper insights into the effect of imposed heating, a set of control experiments was conducted. It can be shown that increasing the temperature of the NaCl solutions often leads to an increase in the output power density. More specifically, the RED device assembled using COF-BTA/PAN and Nafion212 affords an output power density of 21.4 mW cm^{-2} when the temperature of the system is increased by 40 K. The output power density increases to 24.7 mW cm^{-2}, only when the temperatures of the low-concentration side is increased by 40 K, and decreases to 13.1 mW cm^{-2} when the temperature of the high-concentration side is increased by 40 K (Figure S22). These phenomena can be rationalized as follows: Increasing the temperature of the system accelerates the movement of ions, thereby increasing the current and the accompanying output power density (Figure S23). However, because ions spontaneously move from the low- to high-temperature sides, according to the principle of increasing entropy, heating the dilute solution to introduce a temperature gradient ensures that the heat-driven ion transport is in the same direction as that of the salinity gradient, resulting in the largest increases in the current and voltage among the tested conditions.

Long-term stability of the system is critical for practical applications. It takes <1 min to collect an $I-V$ curve for calculating the output power density, during which the system can be considered as existing in a quasi-steady state. For long-term operation, the deleterious effects of convection and temperature polarization cannot be ignored. To address these concerns, a dynamic flow cell was adopted, whereby the electrolyte solutions were circulated using a peristaltic pump to maintain the steady ionic strengths of each reservoir. The stability evaluation shows that the power density does not decrease within 14 days of operation, as exemplified by the RED stack paired with COF-BTA/PAN and Nafion212 (Figure S24).

A family of isoreticular COF membranes with varied charge populations was investigated for use in RED batteries, and the occurrence of ICP during the process of separation was confirmed. The relationship between membrane charge density and permselectivity was corroborated by a combination of experimental data and rigorous numerical simulations. The introduction of a temperature gradient was found to be a simple and reliable strategy to alleviate the ICP phenomenon during RED. The increase in temperature amplified the thermophoretic mobility of ions and consequently decreased the ion-transport resistance. This research is anticipated to provide an alternative strategy for alleviating CP, while simultaneously offering an avenue to utilize untapped low-grade heat energy.

■ ASSOCIATED CONTENT

Supporting Information

The Supporting Information is available free of charge at https://pubs.acs.org/doi/10.1021/acsenergylett.2c01681.

Materials synthesis, characterization details, supporting data, and supporting Figures S1−S24 and Tables S1−S5 (PDF)

■ AUTHOR INFORMATION

Corresponding Author

Qi Sun − *Zhejiang Provincial Key Laboratory of Advanced Chemical Engineering Manufacture Technology, College of Chemical and Biological Engineering, Zhejiang University, Hangzhou 310027, China;* orcid.org/0000-0002-1698-8741; Email: sunqichs@zju.edu.cn

Authors

Changjia Zhu − *Zhejiang Provincial Key Laboratory of Advanced Chemical Engineering Manufacture Technology, College of Chemical and Biological Engineering, Zhejiang University, Hangzhou 310027, China; Department of Chemistry, University of North Texas, Denton, Texas 76201, United States*

Xiuhui Zuo − *Zhejiang Provincial Key Laboratory of Advanced Chemical Engineering Manufacture Technology, College of Chemical and Biological Engineering, Zhejiang University, Hangzhou 310027, China*

Weipeng Xian − *Zhejiang Provincial Key Laboratory of Advanced Chemical Engineering Manufacture Technology, College of Chemical and Biological Engineering, Zhejiang University, Hangzhou 310027, China*

Qing Guo − *Zhejiang Provincial Key Laboratory of Advanced Chemical Engineering Manufacture Technology, College of Chemical and Biological Engineering, Zhejiang University, Hangzhou 310027, China*

Qing-Wei Meng − *Zhejiang Provincial Key Laboratory of Advanced Chemical Engineering Manufacture Technology, College of Chemical and Biological Engineering, Zhejiang University, Hangzhou 310027, China*

Sai Wang − *Zhejiang Provincial Key Laboratory of Advanced Chemical Engineering Manufacture Technology, College of Chemical and Biological Engineering, Zhejiang University, Hangzhou 310027, China*

Shengqian Ma − *Department of Chemistry, University of North Texas, Denton, Texas 76201, United States;* orcid.org/0000-0002-1897-7069

Complete contact information is available at: https://pubs.acs.org/10.1021/acsenergylett.2c01681

Author Contributions

C.Z. and X.Z. contributed equally to this work.

Notes

The authors declare no competing financial interest.

■ ACKNOWLEDGMENTS

The authors acknowledge the National Science Foundation of China (22072132) for financial support of this work.

■ REFERENCES

(1) Zangle, T. A.; Mani, A.; Santiago, J. G. Theory and experiments of concentration polarization and ion focusing at microchannel and nanochannel interfaces. *Chem. Soc. Rev.* **2010**, *39*, 1014−1035.

(2) abu-Rjal, R.; Chinaryan, V.; Bazant, M. Z.; Rubinstein, I.; Zaltzman, B. Effect of concentration polarization on permselectivity. *Phys. Rev. E* **2014**, *89*, 012302.

(3) Cao, L.; Xiao, F.; Feng, Y.; Zhu, W.; Geng, W.; Yang, J.; Zhang, X.; Li, N.; Guo, W.; Jiang, L. Anomalous channel-length dependence in nanofluidic osmotic energy conversion. *Adv. Funct. Mater.* **2017**, *27*, 1604302.

(4) Gray, G. T.; McCutcheon, J. R.; Elimelech, M. Internal concentration polarization in forward osmosis: role of membrane orientation. *Desalination* **2006**, *197*, 1−8.

(5) Man, Z.; Safaei, J.; Zhang, Z.; Wang, Y.; Zhou, D.; Li, P.; Zhang, X.; Jiang, L.; Wang, G. Serosa-mimetic nanoarchitecture membranes for highly efficient osmotic energy generation. *J. Am. Chem. Soc.* **2021**, *143*, 16206−16216.

(6) Zhu, Y.; Zhan, K.; Hou, X. Interface design of nanochannels for energy utilization. *ACS Nano* **2018**, *12*, 908−911.

(7) Ramon, G. Z.; Feinberg, B. J.; Hoek, E. M. V. Membrane-based production of salinity-gradient power. *Energy Environ. Sci.* **2011**, *4*, 4423−4434.

(8) Kim, T.; Rahimi, M.; Logan, B. E.; Gorski, C. A. Harvesting energy from salinity differences using battery electrodes in a concentration flow cell. *Environ. Sci. Technol.* **2016**, *50*, 9791−9797.

(9) Zhang, Z.; Wen, L.; Jiang, L. Nanofluidics for osmotic energy conversion. *Nat. Rev. Mater.* **2021**, *6*, 622−639.

(10) Zhang, Y.; Xiong, T.; Suresh, L.; Qu, H.; Zhang, X.; Zhang, Q.; Yang, J.; Tan, S. C. Guaranteeing complete salt rejection by channeling saline water through fluidic photothermal structure toward synergistic zero energy clean water production and *in situ* energy generation. *ACS Energy Lett.* **2020**, *5*, 3397−3404.

(11) Zhang, Y.; Zhang, H.; Xiong, T.; Qu, H.; Koh, J. J.; Nandakumar, D. K.; Wang, J.; Tan, S. C. Manipulating unidirectional fluid transportation to drive sustainable solar water extraction and brine-drenching induced energy generation. *Energy Environ. Sci.* **2020**, *13*, 4891−4902.

(12) Zhang, Y.; Guo, S.; Yu, Z. G.; Qu, H.; Sun, W.; Yang, J.; Suresh, L.; Zhang, X.; Koh, J. J.; Tan, S. T. An asymmetric hygroscopic structure for moisture-driven hygro-ionic electricity generation and storage. *Adv. Mater.* **2022**, *34*, 2201228.

(13) Logan, B. E.; Elimelech, M. Membrane-based processes for sustainable power generation using water. *Nature* **2012**, *488*, 313−319.

(14) Liu, X.; He, M.; Calvani, D.; Qi, H.; Gupta, K. B. S. S.; de Groot, H. J. M.; Sevink, G. J. A.; Buda, F.; Kaiser, U.; Schneider, G. F. Power generation by reverse electrodialysis in a single-layer nanoporous membrane made from core-rim polycyclic aromatic hydrocarbons. *Nat. Nanotechnol.* **2020**, *15*, 307−312.

(15) Sun, Y.; Wu, Y.; Hu, Y.; Zhu, C.; Guo, H.; Kong, X.-Y.; Luo, E.; Jiang, L.; Wen, L. Thermoenhanced osmotic power generator via lithium bromide and asymmetric sulfonated poly(ether ether ketone)/poly(ether sulfone) nanofluidic membrane. *NPG Asia Mater.* **2021**, *13*, 50.

(16) Wu, Y.; Xin, W.; Kong, X.-Y.; Chen, J.; Qian, Y.; Sun, Y.; Zhao, X.; Chen, W.; Jiang, L.; Wen, L. Enhanced ion transport by graphene oxide/cellulose nanofibers assembled membranes for high-performance osmotic energy harvesting. *Mater. Horiz.* **2020**, *7*, 2702−2709.

(17) Xin, W.; Xiao, H.; Kong, X.-Y.; Chen, J.; Yang, L.; Niu, B.; Qian, Y.; Teng, Y.; Jiang, L.; Wen, L. Biomimetic nacre-like silk-crosslinked membranes for osmotic energy harvesting. *ACS Nano* **2020**, *14*, 9701−9710.

(18) Wang, L.; Wang, Z.; Patel, S. K.; Lin, S.; Elimelech, M. Nanopore-based power generation from salinity gradient: why it is not viable. *ACS Nano* **2021**, *15*, 4093−4107.

(19) Zhu, X.; Hao, J.; Bao, B.; Zhou, Y.; Zhang, H.; Pang, J.; Jiang, Z.; Jiang, L. Unique ion rectification in hypersaline environment: a high-performance and sustainable power generator system. *Sci. Adv.* **2018**, *4*, eaau1665.

(20) Gao, J.; Liu, X.; Jiang, Y.; Ding, L.; Jiang, L.; Guo, W. Understanding the giant gap between single-pore-and membrane-based nanofluidic osmotic power generators. *Small* **2019**, *15*, 1804279.

(21) Chen, J.; Xin, W.; Chen, W.; Zhao, X.; Qian, Y.; Kong, X.-Y.; Jiang, L.; Wen, L. Biomimetic nanocomposite membranes with ultrahigh ion selectivity for osmotic power conversion. *ACS Cent. Sci.* **2021**, *7*, 1486−1492.

(22) Zhang, Z.; Yang, S.; Zhang, P.; Zhang, J.; Chen, G.; Feng, X. Mechanically strong MXene/Kevlar nanofiber composite membranes as high-performance nanofluidic osmotic power generators. *Nat. Commun.* **2019**, *10*, 2920.

(23) Hsu, J.-P.; Su, T.-C.; Peng, P.-H.; Hsu, S.-C.; Zheng, M.-J.; Yeh, L.-H. Unraveling the anomalous surface-charge-dependent osmotic power using a single funnel-shaped nanochannel. *ACS Nano* **2019**, *13*, 13374−13381.

(24) Cho, I.; Sung, G. Y.; Kim, S. J. Overlimiting current through ion concentration polarization layer: hydrodynamic convection effects. *Nanoscale* **2014**, *6*, 4620−4626.

(25) Kandambeth, S.; Dey, K.; Banerjee, R. Covalent organic frameworks: chemistry beyond the structure. *J. Am. Chem. Soc.* **2019**, *141*, 1807−1822.
(26) He, X.; Yang, Y.; Wu, H.; He, G.; Xu, Z.; Kong, Y.; Cao, L.; Shi, B.; Zhang, Z.; Tongsh, C.; Jiao, K.; Zhu, K.; Jiang, Z. De novo design of covalent organic framework membranes toward ultrafast anion transport. *Adv. Mater.* **2020**, *32*, 2001284.
(27) Chen, S.; Zhu, C.; Xian, W.; Liu, X.; Liu, X.; Zhang, Q.; Ma, S.; Sun, Q. Imparting ion selectivity to covalent organic framework membranes using de novo assembly for blue energy harvesting. *J. Am. Chem. Soc.* **2021**, *143*, 9415−9422.
(28) Yuan, C.; Wu, X.; Gao, R.; Han, X.; Liu, Y.; Long, Y.; Cui, Y. Nanochannels of covalent organic frameworks for chiral selective transmembrane transport of amino acids. *J. Am. Chem. Soc.* **2019**, *141*, 20187−20197.
(29) Xian, W.; Zhang, P.; Zhu, C.; Zuo, X.; Ma, S.; Sun, Q. Bionic thermosensation inspired temperature gradient sensor based on covalent organic framework nanofluidic membrane with ultrahigh sensitivity. *CCS Chem.* **2021**, *3*, 2464−2472.
(30) Li, Y.; Wu, Q.; Guo, X.; Zhang, M.; Chen, B.; Wei, G.; Li, X.; Li, X.; Li, S.; Ma, L. Laminated self-standing covalent organic framework membrane with uniformly distributed subnanopores for ionic and molecular sieving. *Nat. Commun.* **2020**, *11*, 599.
(31) Sheng, F.; Wu, B.; Li, X.; Xu, T.; Shehzad, M. A.; Wang, X.; Ge, L.; Wang, H.; Xu, T. Efficient ion sieving in covalent organic framework membranes with sub-2-nanometer channels. *Adv. Mater.* **2021**, *33*, 2104404.
(32) Bing, S.; Xian, W.; Chen, S.; Song, Y.; Hou, L.; Liu, X.; Ma, S.; Sun, Q.; Zhang, L. Bio-inspired construction of ion conductive pathway in covalent organic framework membranes for efficient lithium extraction. *Matter* **2021**, *4*, 2027−2038.
(33) Colson, J. W.; Woll, A. R.; Mukherjee, A.; Levendorf, M. P.; Spitler, E. L.; Shields, V. B.; Spencer, M. G.; Park, J.; Dichtel, W. R. Oriented 2D covalent organic framework thin films on single-layer graphene. *Science* **2011**, *332*, 228−231.
(34) Hao, Q.; Li, Z.-J.; Lu, C.; Sun, B.; Zhong, Y.-W.; Wan, L.-J.; Wang, D. Oriented two-dimensional covalent organic framework films for near-infrared electrochromic application. *J. Am. Chem. Soc.* **2019**, *141*, 19831−19838.
(35) Zhang, P.; Chen, S.; Zhu, C.; Hou, L.; Xian, W.; Zuo, X.; Zhang, Q.; Zhang, L.; Ma, S.; Sun, Q. Covalent organic framework nanofluidic membrane as a platform for highly sensitive bionic thermosensation. *Nat. Commun.* **2021**, *12*, 1844.
(36) Hou, S.; Ji, W.; Chen, J.; Teng, Y.; Wen, L.; Jiang, L. Free-standing covalent organic framework membrane for high-efficiency salinity gradient energy conversion. *Angew. Chem., Int. Ed.* **2021**, *60*, 9925−9930.
(37) Fan, H.; Peng, M.; Strauss, I.; Mundstock, A.; Meng, H.; Caro, J. High-flux vertically aligned 2D covalent organic framework membrane with enhanced hydrogen separation. *J. Am. Chem. Soc.* **2020**, *142*, 6872−6877.
(38) Zuo, X.; Zhu, C.; Xian, W.; Meng, Q.-W.; Guo, Q.; Zhu, X.; Wang, S.; Wang, Y.; Ma, S.; Sun, Q. Thermo-osmotic energy conversion enabled by covalent-organic-framework membranes with record output power density. *Angew. Chem., Int. Ed.* **2022**, *61*, e202116910.
(39) Shinde, D. B.; Sheng, G.; Li, X.; Ostwal, M.; Emwas, A.-H.; Huang, K.-W.; Lai, Z. Crystalline 2D covalent organic framework membranes for high-flux organic solvent nanofiltration. *J. Am. Chem. Soc.* **2018**, *140*, 14342−14349.
(40) Ying, Y.; Peh, S. B.; Yang, H.; Yang, Z.; Zhao, D. Ultrathin covalent organic framework membranes via a multi-interfacial engineering strategy for gas separation. *Adv. Mater.* **2022**, *34* (25), 2104946.
(41) Liu, L.; Yin, L.; Cheng, D.; Zhao, S.; Zang, H.-Y.; Zhang, N.; Zhu, G. Surface-mediated construction of an ultrathin free-standing covalent organic framework membrane for efficient proton conduction. *Angew. Chem., Int. Ed.* **2021**, *60*, 14875−14880.
(42) Zhao, S.; Jiang, C.; Fan, J.; Hong, S.; Mei, P.; Yao, R.; Liu, Y.; Zhang, S.; Li, H.; Zhang, H.; Sun, C.; Guo, Z.; Shao, P.; Zhu, Y.; Zhang, J.; Guo, L.; Ma, Y.; Zhang, J.; Feng, X.; Wang, F.; Wu, H.; Wang, B. Hydrophilicity gradient in covalent organic frameworks for membrane distillation. *Nat. Mater.* **2021**, *20*, 1551−1558.
(43) Zhu, C.; Xian, W.; Song, Y.; Zuo, X.; Wang, Y.; Ma, S.; Sun, Q. Manipulating charge density in nanofluidic membranes for optimal osmotic energy production density. *Adv. Funct. Mater.* **2022**, *32*, 2109210.
(44) Lin, C.-Y.; Combs, C.; Su, Y.-S.; Yeh, L.-H.; Siwy, Z. S. Rectification of concentration polarization in mesopores leads to high conductance ionic diodes and high performance osmotic power. *J. Am. Chem. Soc.* **2019**, *141*, 3691−3698.
(45) Kim, S. J.; Ko, S. H.; Kwak, R.; Posner, J. D.; Kang, K. H.; Han, J. Multi-vortical flow inducing electrokinetic instability in ion concentration polarization layer. *Nanoscale* **2012**, *4*, 7406−7410.
(46) Lindley, D. The energy should always work twice. *Nature* **2009**, *458*, 138−141.
(47) Xie, G.; Li, P.; Zhang, Z.; Xiao, K.; Kong, X.-Y.; Wen, L.; Jiang, L. Skin-inspired low-grade heat energy harvesting using directed ionic flow through conical nanochannels. *Adv. Energy Mater.* **2018**, *8*, 1800459.
(48) Li, Z.-Q.; Wu, Z.-Q.; Ding, X.-L.; Wu, M.-Y.; Xia, X.-H. A solar thermoelectric nanofluidic device for solar thermal energy harvesting. *CCS Chem.* **2021**, *3* (7), 2174−2182.
(49) Chen, K.; Yao, L.; Yan, F.; Liu, S.; Yang, R.; Su, B. Thermo-osmotic energy conversion and storage by nanochannels. *J. Mater. Chem. A* **2019**, *7*, 25258−25261.
(50) Catrini, P.; Cipollina, A.; Micale, G.; Piacentino, A.; Tamburini, A. Potential applications of salinity gradient power-heat engines for recovering low-temperature waste heat in cogeneration plants. *Energy Convers. Manag.* **2021**, *237*, 114135.
(51) Palenzuela, P.; Micari, M.; Ortega-Delgado, B.; Giacalone, F.; Zaragoza, G.; Alarcón-Padilla, D.; Cipollina, A.; Tamburini, A.; Micale, G. Performance analysis of a RED-MED salinity gradient heat engine. *Energies* **2018**, *11*, 3385.
(52) Straub, A. P.; Elimelech, M. Energy efficiency and performance limiting effects in thermo-osmotic energy conversion from low-grade heat. *Environ. Sci. Technol.* **2017**, *51*, 12925−12937.
(53) Duan, J.; Yu, B.; Huang, L.; Hu, B.; Xu, M.; Feng, G.; Zhou, J. Liquid-state thermocells: opportunities and challenges for low-grade heat harvesting. *Joule* **2021**, *5*, 768−779.
(54) Wu, C.; Xiao, T.; Tang, J.; Zhang, Q.; Liu, Z.; Liu, J.; Wang, H. Biomimetic temperature-gated 2D cationic nanochannels for controllable osmotic power harvesting. *Nano energy* **2020**, *76*, 105113.
(55) Zhou, W.; Yamamoto, K.; Miura, A.; Iguchi, R.; Miura, Y.; Uchida, K.-i.; Sakuraba, Y. Seebeck-driven transverse thermoelectric generation. *Nat. Mater.* **2021**, *20*, 463−467.
(56) Li, T.; Zhang, X.; Lacey, S. D.; Mi, R.; Zhao, X.; Jiang, F.; Song, J.; Liu, Z.; Chen, G.; Dai, J.; Yao, Y.; Das, S.; Yang, R.; Briber, R. M.; Hu, L. Cellulose ionic conductors with high differential thermal voltage for low-grade heat harvesting. *Nat. Mater.* **2019**, *18*, 608−613.
(57) Straub, A. P.; Yip, N. Y.; Lin, S.; Lee, J.; Elimelech, M. Harvesting low-grade heat energy using thermo-osmotic vapour transport through nanoporous membranes. *Nat. Energy* **2016**, *1* (7), 16090.
(58) Lee, S. W.; Yang, Y.; Lee, H.-W.; Ghasemi, H.; Kraemer, D.; Chen, G.; Cui, Y. An electrochemical system for efficiently harvesting low-grade heat energy. *Nat. Commun.* **2014**, *5*, 3942.
(59) Wang, Y.; Liu, C.; Wang, Y.; Zhu, C.; Chen, X.; Liu, B. Efficient photo-thermo-electric conversion using polyoxovanadate in ionic liquid for low-grade heat utilization. *ChemSusChem* **2021**, *14*, 5434−5441.

https://doi.org/10.1021/acsenergylett.2c01681
ACS Energy Lett. 2022, 7, 2937−2943